Mon. Not. R. Astron. Soc. **000**, 1–?? (2019) Printed 28 July 2019 (MN LATEX style file v2.2)

MOBSTER - III. HD 62658, the second magnetic chemically peculiar eclipsing binary

M. E. Shultz[1⋆†], C. Johnston[2], J. Labadie-Bartz[3], V. Petit[1] A. David-Uraz[1], O. Kochukhov[4],, G. A. Wade[5]

[1] *Department of Physics and Astronomy, University of Delaware, 217 Sharp Lab, Newark, Delaware, 19716, USA*
[2] *Instituut voor Sterrenkunde, KU Leuven, Celestijnenlaan 200D, 3001, Leuven, Belgium*
[3] *Instituto de Astronomia, Geofísica e Ciencias Atmosféricas, Universidade de Sào Paulo, Rua do Matão 1226, Cidade Universitãria, Sáo Paulo, SP 05508-900, Brazil*
[4] *Department of Physics and Astronomy, Uppsala University, Box 516, Uppsala 75120, Sweden*
[5] *Department of Physics and Space Science, Royal Military College of Canada, Kingston, Ontario K7K 7B4, Canada*

ABSTRACT

HD 62658 (B9p) is a little-studied chemically peculiar star. Light curves obtained by the Kilodegree Extremely Little Telescope (KELT) and Transiting Exoplanet Survey Satellite (TESS) show clear eclipses with a period of about 4.75 d, as well as out-of-eclipse brightness modulations with the same period consistent with rotational modulation of surface chemical spots. High-resolution ESPaDOnS circular spectropolarimetry shows a clear Zeeman signature in the line profile of the primary; there is no indication of a magnetic field in the secondary. PHOEBE modelling of the light curve and radial velocities indicates that the two components have almost identical masses of about 3 $M_{\odot}$. The primary's longitudinal magnetic field $\langle B_z \rangle$ varies between about +100 and −250 G, suggesting a surface magnetic dipole strength $B_{\rm d} = 850$ G. Bayesian analysis of the Stokes V profiles indicates $B_{\rm d} = 650$ G for the primary and $B_{\rm d} < 110$ G for the secondary. The primary's line profiles are highly variable, consistent with the hypothesis that the out-of-eclipse brightness modulation is a consequence of rotational modulation of that star's chemical spots. We also detect pulsation frequencies in the light curve, which we tentatively assign to the secondary on the basis of its own weak line profile variations. This system represents an excellent opportunity to examine the consequences of magnetic fields for stellar structure via comparison of two stars that are identical with the exception that one is magnetic. The existence of such a system furthermore suggests that fossil magnetic fields may form during the pre-main sequence due to a magnetic bistability mechanism analagous to that observed in M dwarves.

Key words: stars: individual: HD 62658 – stars: early-type – stars: magnetic field – stars: binaries: eclipsing – stars: chemically peculiar

1 INTRODUCTION

Magnetic fields are found in about 10% of stars with radiative envelopes (Grunhut et al. 2017; Sikora et al. 2019a). These magnetic fields are typically strong (above 300 G: Aurière et al. 2007; Sikora et al. 2019b), globally organized (usually dipolar, e.g. Shultz et al. 2018b; Kochukhov et al. 2019), and stable over a timescale of decades (e.g. Shultz et al. 2018b). These properties, together with the absence of any obvious dependence of surface magnetic field strength upon rotation as would be expected for the dynamo-sustained magnetic fields of cool stars, leads to the characterization of hot star magnetic fields as so-called "fossil" magnetic fields (e.g. Neiner et al. 2015, and references therein).

It is extraordinarily rare to find a magnetic early-type star in a close binary system. The Binarity and Magnetic Interactions in various classes of Stars (BinaMIcS) survey found an incidence rate of magnetic stars in close binaries below 2% across the population of upper main sequence multiple systems (Alecian et al. 2015). This is a surprising result given that the binary fraction of hot stars is very high (e.g. Sana et al. 2012; de Mink et al. 2014). It has been suggested

⋆ E-mail: mshultz@udel.edu
† Annie Jump Cannon Fellow

that this rarity might be related to the formation mechanism for fossil magnetic fields. For instance, if fossil magnetic flux is inherited and amplified from the molecular cloud in which the star is born, strong magnetic fields might inhibit cloud fragmentation and, thus, prevent the formation of close binary systems (Commerçon et al. 2011). Alternatively, fossil fields might be left over from dynamos generated during stellar mergers, an observation compatible with the apparent anomalous youth of some magnetic stars (Schneider et al. 2016) as well as with the expected rate of mergers (de Mink et al. 2013, 2014). It has also been suggested that the tidal influence of a close companion may lead to rapid decay of fossil magnetic fields (Vidal et al. 2019).

Since only a handful of magnetic close binaries are known (a list is provided by Landstreet et al. 2017), there is value in both increasing the sample of such stars, as well as closely studying the known systems. Recently, examination of the the Kilodegree Extremely Little Telescope (KELT; Pepper et al. 2007) light-curve of the little-studied star HD 62658 revealed the presence of eclipses as well as out-of-eclipse brightness modulations. This pattern is very similar to that observed in the only known eclipsing binary Ap star, HD 66051 (Kochukhov et al. 2018). Since HD 62658 is listed as a chemically peculiar (CP) Bp star in the Renson & Manfroid (2009) *Catalogue of Ap, HgMn and Am stars*, we obtained high-resolution spectropolarimetric observations in order to search for the presence of a magnetic field.

The primary goal of the study presented here, which is the third of a series of planned publications by the MOBSTER Collaboration[1], is to provide a first characterisation of HD 62658. In the following we report the results of our observations, together with the recently obtained Transiting Exoplanet Survey Satellite (TESS) light curve. In § 2 we describe the photometric and spectropolarimetric datasets. The KELT and TESS light curves are analysed in § 3. Magnetometry is presented in § 4. The implications of our results are presented in § 5, and our conclusions are summarized in § 6.

2 OBSERVATIONS

2.1 Photometry

2.1.1 KELT

The Kilodegree Extremely Little Telescope (KELT) is a photometric survey comprising two similar telescopes. KELT-North (Pepper et al. 2007) is located at Winer Observatory in Sonoita, Arizona, and KELT-South (Pepper et al. 2012) is situated at the South African Astronomical Observatory in Sutherland, South Africa. Both telescopes have a 42 mm aperture, a 26° x 26° field of view, and a pixel scale of 23″. The KELT survey is designed to detect giant exoplanets transiting stars between $8 \lesssim V \lesssim 11$, and is well-suited for detecting periodic signals in stellar light curves down to amplitudes of a few mmag **(cite BCEP paper once submitted)**. The single passband of the KELT telescopes is roughly equivalent to a broadband $V + R + I$ filter. The normal telescope operations are completely automated and observations are made nightly. HD 62658 was observed 2730 times with KELT-South between 2013 May 11 – 2017 Oct 1 with a median cadence of 31 minutes, covering 337 cycles over the observational baseline.

Part of the KELT strategy for discovering transiting exoplanets involves an algorithm that pre-selects potential exoplanet candidates from reduced light curves for all sources identified in a given field (Collins et al. 2018). HD 62658 was one such source identified in this way. However, the light curve clearly shows eclipses of two different depths, and is thus an eclipsing binary. The out-of-eclipse variability apparent in the light curve is inconsistent with ellipsoidal variation, and a rotational origin was suspected, prompting further investigation.

The KELT data are shown in the top panel of Fig. 1. Using the Python package astropy (Astropy Collaboration et al. 2013; Price-Whelan et al. 2018), a Lomb-Scargle (Lomb 1976; Zechmeister & Kürster 2009) frequency analysis of the data using a single Fourier term reveals a periodogram with many peaks (bottom panel of Figure 1), including that associated with the 0.21043(4) d^{-1} orbital frequency. Inspection of the light curve phased to the remaining peaks reveals that they are either harmonics of the orbital period or are aliases induced by the observing strategy of KELT (the most prominent being at 1 and 2 d^{-1}).

2.1.2 TESS

Launched on 18 April 2018, TESS seeks to discover new exoplanets by surveying about ∼85% of the sky over its 2-year nominal mission, divided into 26 partially overlapping "sectors" (each corresponding to a total field of view of 24°×96° across the four cameras onboard; the pixel size is 21") that are each observed for ∼ 27 d (Ricker et al. 2015). The TESS bandpass is broad and covers a range of approximately 6,000-10,000 Å. Full-frame images (FFIs) are acquired every 30 minutes. Over 500 million point sources fall into at least one of these sectors (and are thus included in the TESS Input Catalog, or TIC), and out of these, ∼ 200,000 were selected for 2-minute cadence observations (Stassun et al. 2018).

HD 62658 (= TIC 149319411) is one such target, and was observed by TESS in sectors 7 and 8 (7 Jan. 2019 - 28 Feb. 2019; observing programs G011127 and G011060, PI Ricker). Although no contamination ratio is available for this star in the TIC, it is the brightest star by about 2.5 mag in the TESS bandpass within a radius of 3.5'; therefore, the variations seen in the TESS light curve are likely intrinsic to HD 62658. The observations for this star were downloaded from the Mikulski Archive for Space Telescopes (MAST)[2] and we used the `PDCSAP` flux column from the light curve files generated by the TESS Science Processing Operations Center (Jenkins et al. 2016).

Upon an initial investigation of the TESS light curves, we found the sector 7 photometry to be well behaved, while the sector 8 data exhibited strong instrumental trends near the gaps that are present between sectors and in the middle of each sector. Taking into account data points marked

[1] Magnetic OB[A] Stars with TESS: probing their Evolutionary and Rotational properties; David-Uraz et al. 2019

[2] `http://archive.stsci.edu/`

as poor-quality in the TESS light curve files, the sector 8 data also features a significantly larger middle gap (5.9 d) compared to the sector 7 observations (1.7 d). Because of the time scales associated with the different sources of variability described in § 3, properly detrending these artefacts without affecting the signals we are attempting to model would prove to be quite difficult, and as such, we consider this effort to lie outside the scope of this initial discovery paper. Therefore, we choose to only take into account the data acquired in sector 7. This decision does not severely impact the scientific yield of our study, as the exquisite data quality of the TESS light curve allows us to detect low amplitude signals, while the long temporal baseline of the KELT data can be leveraged to accomplish a very precise orbital period determination. The sector 7 data are shown together with the KELT data in the top panel of Fig. 1.

2.2 Spectropolarimetry

Between 15/03/2019 and 22/03/2019 six spectropolarimetric circular polarization (Stokes V) sequences of HD 62658 were obtained with the ESPaDOnS instrument at the Canada-France-Hawaii Telescope (CFHT) under program code 19AC19. ESPaDOnS is a high-resolution ($\lambda/\Delta\lambda \sim 65,000$ at 500 nm) echelle spectropolarimeter covering the spectral range between 370 and 1000 nm across 40 spectral orders. The reduction and analysis of ESPaDOnS data were described in detail by Wade et al. (2016). Each observation consists of 4 unpolarized Stokes I spectra, one Stokes V spectrum, and two diagnostic null N spectra obtained by combining the different polarizations in such a way as to cancel out the intrinsic polarization of the source.

A uniform sub-exposure time of 597 s was used for each sub-exposure, with the total exposure time across the sequence 4× this number. The mean peak per pixel signal-to-noise (S/N) in the dataset is 261; all 6 observations are of comparable quality.

Each observation was post-processed by normalizing each spectral order using polynomial splines fit by eye to the continuum, thus ensuring the continuum assumed by least-squares deconvolution is as close as possible to unity, while avoiding as much as possible over-normalization due to broad features such as H Balmer wings at the edges of spectral orders.

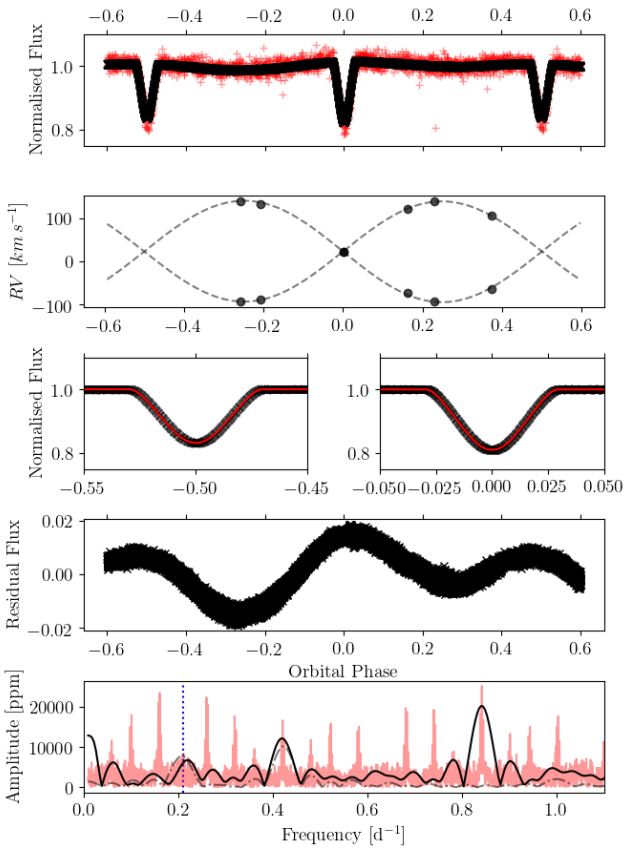

Figure 1. *First Row*: Phase folded TESS lightcurve (black) and KELT lightcurve (red). *Second Row*: Phase folded RV observations (black circles) with optimized RV curves(dashed black lines). *Third Row*: Zoom in of primary (right panel) and secondary (left panel) eclipse with optimized model (red). *Fourth Row*: Residual lightcurve after removal of binary model, phase folded over the orbital period. *Bottom Row*:Periodograms of the original KELT data (red), original TESS data (black), and TESS data after removal of the binary model (dashed grey). The orbital frequency is denoted by vertical blue dashed line. Harmonics of the main period and multiple aliases are apparent, especially associated with the diurnal observing strategy of KELT.

3 LIGHT CURVE ANALYSIS

In order to obtain dynamic mass and radius estimates for the components of this system, we perform light curve modelling with the PHOEBE binary modelling code (Prša & Zwitter 2005; Prsa et al. 2011) following the framework of Kochukhov et al. (2018), which we briefly summarise below.

3.1 Signal Separation

Inspection of the TESS lightcurve reveals both eclipses and apparent spot modulation. Phase folding the lightcurve on the orbital period reveals that spot signal is nearly commensurate with the orbital period. Although PHOEBE can model spots, their inclusion in the modelling process can become highly degenerate without stringent constraints. As the spectroscopic dataset here cannot produce the location, size, temperature, and multiplicity constraints required by photometric spot modelling, we choose to model the spot signal as a harmonic series instead. Since the amplitude of the spot signal is of the same order as the orbital signal, we must disentangle the two iteratively. As a first approach, we clip the eclipses and fit a harmonic series to the remaining signal via non-linear least squares, which is then removed from the original lightcurve. Then, a binary model is optimised on these residuals. The binary model is then removed from the original lightcurve, and we fit a harmonic series to these residuals. A new binary model is optimised and the process is repeated until there is no change in the resulting fit. Since we remove a non-physical harmonic series from the lightcurve, we fix the albedos and gravity brightening exponents per component to unity.

Parameter		Prior Range	HPD Estimate
$T_0 - 2456425$	d	(-2,2)	$0.231^{+0.005}_{-0.006}$
$P_{\rm orb}$	d	(4,6)	4.752212^{+1e-5}_{-9e-6}
q	$\frac{M_2}{M_1}$	(0.5,1.5)	$1.012^{+0.006}_{-0.007}$
a	$R_\odot$	(10,30)	$22.041^{+0.001}_{-0.001}$
γ	$\mathrm{km\,s^{-1}}$	(-50,50)	$22.8^{+0.4}_{-0.4}$
i	deg	(70,90)	$83.6027^{+0.01}_{-0.008}$
$e\cos\omega_0$		(-0.1,0.1)	0.00022^{+1e-5}_{-1e-5}
$e\sin\omega_0$		(-0.1,0.1)	$0.0042^{+0.0004}_{-0.0004}$
$T_{\rm eff,1}$	K	N/A	12 500
$T_{\rm eff,2}/T_{\rm eff,1}$		(0.5,1.5)	$0.9385^{+0.005}_{-0.005}$
Ω_1		(5,20)	$10.58^{+0.01}_{-0.01}$
Ω_2		(5,20)	$10.39^{+0.06}_{-0.05}$
$\omega_{rot,1}/\omega_{orb}$		(0.2,5)	$1.07^{+0.05}_{-0.06}$
$\omega_{rot,2}/\omega_{orb}$		(0.2,5)	$0.81^{+0.03}_{-0.03}$
l_1	%	(20,80)	$51.1^{+0.2}_{-0.2}$
l_3	%	(0,20)	$2.2^{+0.3}_{-0.3}$

Table 1. Table listing varied parameters during the MCMC optimisation. Median values for all parameters with errors listed as the boundaries taken from 68.27% HPD intervals.

Parameter		Estimate
e		$0.0042^{+0.0004}_{-0.0004}$
ω_0	rad	$1.519^{+0.005}_{-0.005}$
r_2/r_1		$1.031^{+0.002}_{-0.002}$
$r_1 + r_2$		$0.2126^{+0.0001}_{-0.0001}$
M_1	$\mathrm{M}_\odot$	$3.16^{+0.01}_{-0.01}$
M_2	$\mathrm{M}_\odot$	$3.20^{+0.01}_{-0.01}$
R_1	$\mathrm{R}_\odot$	$2.307^{+0.002}_{-0.003}$
R_2	$\mathrm{R}_\odot$	$2.238^{+0.003}_{-0.003}$
$\log g_1$	dex	$4.212^{\,0.002}_{-0.002}$
$\log g_2$	dex	$4.191^{\,0.002}_{-0.002}$

Table 2. Geometric and derived parameters and their values as obtained from MCMC modelling.

3.2 Modelling setup

To optimise our solution, the PHOEBE binary modeling code was wrapped into the Bayesian sampling code EMCEE (Foreman-Mackey et al. 2013) which employs an affine-invariant Markov Chain Monte Carlo (MCMC) ensemble sampling approach to numerically evaluate the posterior distribution of a set of sampled parameters. The posterior distribution of a set of sampled parameters, $p\,(\Theta|d)$, is given by Bayes' Theorem:

$$p\,(\Theta|d) \propto \mathcal{L}\,(d|\Theta)\;p\,(\Theta)\,, \qquad (1)$$

where Θ is the vector of sampled parameters which describe the light curve and d are the TESS data. We take the likelihood function $\mathcal{L}\,(d|\Theta)$ to be a χ^2 statistic and encode any previously known information in the priors, $p\,(\Theta)$. The light curve and radial velocity curves were optimised simultaneously (radial velocity measurements were obtained from ESPaDOnS data; see § 4). As mentioned previously, we fixed the albedos and gravity brightening exponents. We fixed the primary effective temperature to 12 500 K and sampled the ratio of the temperatures $T_{\rm eff,2}/T_{\rm eff,1}$. Furthermore, to incorporate as much information as possible, we applied Gaussian posteriors on the projected rotational velocities $v_{1,2}\sin i$ according to those values derived in § 4. Finally, we allowed for an eccentric orbit.

	Frequency [$\mathrm{d^{-1}}$]	Amplitude [ppm]	SNR	Note
f_1	0.21042 ± 0.00004	6985 ± 12	58	
f_2	0.42086 ± 0.00003	8583 ± 13	76	$2f_1$
f_3	1.0023 ± 0.0001	6985 ± 11	23	
f_4	0.5797 ± 0.0004	6985 ± 10	5	

Table 3. Frequencies, amplitudes, and phases extracted from original lightcurve with the optimised binary model removed.

3.3 Modelling results

The sampled parameters, their priors, and their posterior estimates are listed in Table 1. We also report geometric and derived parameter estimates and their errors in Table 2. The parameter estimates are calculated as the median of posterior distribution, while the uncertainties are calculated as 68.27% Highest Posterior Density (HPD) intervals from the marginalised posterior distribution of a given parameter. In the case of normally distributed posteriors, HPD estimates will agree with the mean and 1σ of a Gaussian fit to the distribution. In the event of non-normally distributed posteriors, however, HPD estimates have the advantage of being flexible and being able to capture the breadth of the possible solution space, and are capable of producing asymmetric uncertainties. The marginalised posteriors are shown in the appendix.

The residuals of the best fit model and the original lightcurve are shown in black in the fourth panel of Fig. 1. The red lightcurve shows the residuals after four significant frequencies were pre-whitened from the light curve according to Degroote et al. (2009). The bottom panel shows the Scargle periodogram of the two residual lightcurves in the top panel, with the orbital frequency marked with a vertical dashed blue line. The extracted frequencies are listed in Table 3.

We note that f_1 and f_2 are part of a harmonic series, while f_3 and f_4 are independent signals. Within formal uncertainties, the base frequency f_1 of the signal attributed to spots is the same as $f_{\rm orb} = 0.2104283(4)$. Furthermore, the HPD estimates for the synchronicity parameter $\omega_{\rm rot}/\omega_{\rm orb}$ place the primary as 1.16σ away from rotating synchronously. Thus, it is reasonable to conclude that the primary is nearly if not already rotating synchronously with the orbit, within the errors. We note that the secondary, however, is (according the the synchronicity parameter) rotating sub-synchronously. The derived binary parameters result in the following synchronisation and circularisation timescales: $\log(\tau_{sync}) = 6.708 \pm 0.001$ and $\log(\tau_{circ}) = 9.108 \pm 0.001$ (Zahn 1975, 1977). Since the eccentricity is very close to

zero, and the system has thus evidently had time to circularize, synchronized rotation is to be expected.

As we remove a harmonic series representing the spot signal, and hence the non-baseline light, the estimates of third light are to be considered with caution. The two frequencies f_3 and f_4 occur in frequency regions where gravity mode pulsations are expected in B-type stars, however, due to the uncertain amount of third light, we cannot say for certain that these signals originate from a component of HD 62658.

We note that any structure in the residuals is likely due to the asymmetric blocking and subsequent modulation of light variations from the surface features (spots) and/or the pulsational signal, should this signal originate from a component of this system. One possible means of accounting for this would be to incorporate Gaussian Processes into the modelling procedure, however this is beyond the scope of the discovery paper.

4 MAGNETOMETRY

In order to maximize the precision with which the stars' magnetic fields can be measured, least-squares deconvolution (LSD; Donati et al. 1997) profiles were extracted from the ESPaDOnS spectra using the iLSD package (Kochukhov et al. 2010). The line mask was created from a line list downloaded from the Vienna Atomic Lines Database (VALD3; Piskunov et al. 1995; Ryabchikova et al. 1997; Kupka et al. 1999, 2000; Ryabchikova et al. 2015) with an 'extract stellar' request. We adopted the $\log g = 4.0$ as a reasonable guess and $T_{\rm eff} = 12.3$ kK determined by Glagolevskij (1994), which is consistent with the spectral type of B9p assigned by Renson & Manfroid (2009) in their *Catalogue of Ap, HgMn and Am stars*. We also adopted enhanced Si, Cr, Ti, Fe, Pr, Eu, and Nd abundances, as is typical for intermediate-mass stars showing Ap-type chemical peculiarites. The line depth threshold of the line list is 0.1 below the continuum, as the inclusion of lines weaker than this does not in practice greatly improve the S/N of the LSD profiles, whilst at the same time unreasonably increasing the time taken to extract each profile. The line mask was cleaned using the method described by Shultz et al. (2018b), with 1410 remaining out of the original 2130 lines. LSD profiles were extracted using velocity pixels of 3.6 $\mathrm{km\,s^{-1}}$, or twice the average width of ESPaDOnS pixels, in order to slightly increase the S/N, and a Tikhonov regularization factor of 0.2 was applied in order to reduce the signal degradation associated with cross-correlation (Kochukhov et al. 2010).

The resulting LSD profiles are shown in Fig. 2. The line profiles of the two stellar components are clearly separated in velocity space in five of the observations, and exhibit a variation of about 200 $\mathrm{km\,s^{-1}}$. In one observation (03/21) the line profiles are blended, indicating it was obtained during an eclipse. Radial velocity (RV) measurements obtained from the LSD Stokes I profiles are given in Table 4. RVs were measured using the paramaterized line profile fitting package described by Grunhut et al. (2017), which also provides the projected rotational velocities $v \sin i$: for the primary, 26.2 ± 1.3 $\mathrm{km\,s^{-1}}$, and for the secondary, 20.4 ± 0.7 $\mathrm{km\,s^{-1}}$, where the uncertainties correspond to the standard deviation of the fits across the 5 non-eclipsing observations.

A Zeeman signature is clearly visible in Stokes V in all observations, corresponding to the position of the primary's line profile. Five observations yield a statistical definite detection (DD) inside the primary's line profile, according to the criteria described by Donati et al. (1992, 1997) (i.e. a False Alarm Probability FAP$< 10^{-5}$). Within the secondary's line profile there is no indication of a Zeeman signature, and these observations yield non-detections (NDs) according to the same criteria (FAP$> 10.^{-3}$). This suggests that only the primary is magnetic. Detection flags are given in Table 4.

The observation on 03/21 yields a marginal detection (MD). This observation was obtained when the presumed non-magnetic star was eclipsing the magnetic star, and the MD is likely due to residual light from the magnetic component. As is clear from the light curve, the system is not fully eclipsing, so residual light from the eclipsed component during eclipses is expected.

The right panels of Fig. 2 show the Stokes I line profiles of the two components, from five non-eclipsing observations, shifted to their respective rest frames. The complex structure and asymmetry in the primary's line profiles is consistent with the presence of chemical spots. The secondary, by contrast, shows some signs of variability near the core of the line, albeit much weaker than the variations of the primary. These could be a consequence of the non-radial pulsations identified in the light curve (f_3 and f_4, Table 3). It is clear that the out-of-eclipse variations in the system's light curve are almost certainly due to rotational modulation of the primary's surface chemical abundance inhomogeneities.

4.1 Longitudinal magnetic field

To quantify the strength of the stars' magnetic fields we measured the disk-averaged longitudinal magnetic fields $\langle B_z \rangle$ (Mathys 1989). These are summarized in Table 4. The secondary's $\langle B_z \rangle$ is consistent with zero. The primary varies between about $\langle B_z \rangle$ +100 and −200 G, and 2 of the observations yield $\langle B_z \rangle$ close to zero (with crossover signatures detectable in Stokes V). This indicates we are seeing both magnetic poles and the magnetic equator. The $\langle B_z \rangle$ measurement from the final observation was assigned to the primary, but is not particularly meaningful since the magnetic component is partially obscured.

Fig. 3 shows the $\langle B_z \rangle$ measurements of the two components phased with the rotational frequency f_1 identified from the light curve. The $\langle B_z \rangle$ measurements of the primary vary coherently with this period, increasing confidence that $P_{\rm orb} = P_{\rm rot}$. The measurements were phased using $T_{0,\rm mag} = 2458558.9(2)$, defined at $\langle B_z \rangle = \langle B_z \rangle_{\rm max}$. The small difference between f_1 and $f_{\rm orb}$ makes essentially no difference in the phasing of $\langle B_z \rangle$.

Fitting a first-order sinusoid of the form $\langle B_z \rangle = B_0 + B_1 \sin(\phi + \Phi)$, where ϕ is the rotational phase, yields $B_0 = 6 \pm 9$ G and $B_1 = 316 \pm 21$ G. The r parameter, used to constrain the relationship between $i_{\rm rot}$ and the magnetic obliquity angle β (Preston 1967),

$$r = \frac{|B_0| - B_1}{|B_0| + B_1} = \frac{\cos(i_{\rm rot} + \beta)}{\cos(i_{\rm rot} - \beta)}, \qquad (2)$$

is then $r = -0.96 \pm 0.06$. To determine the star's oblique ro-

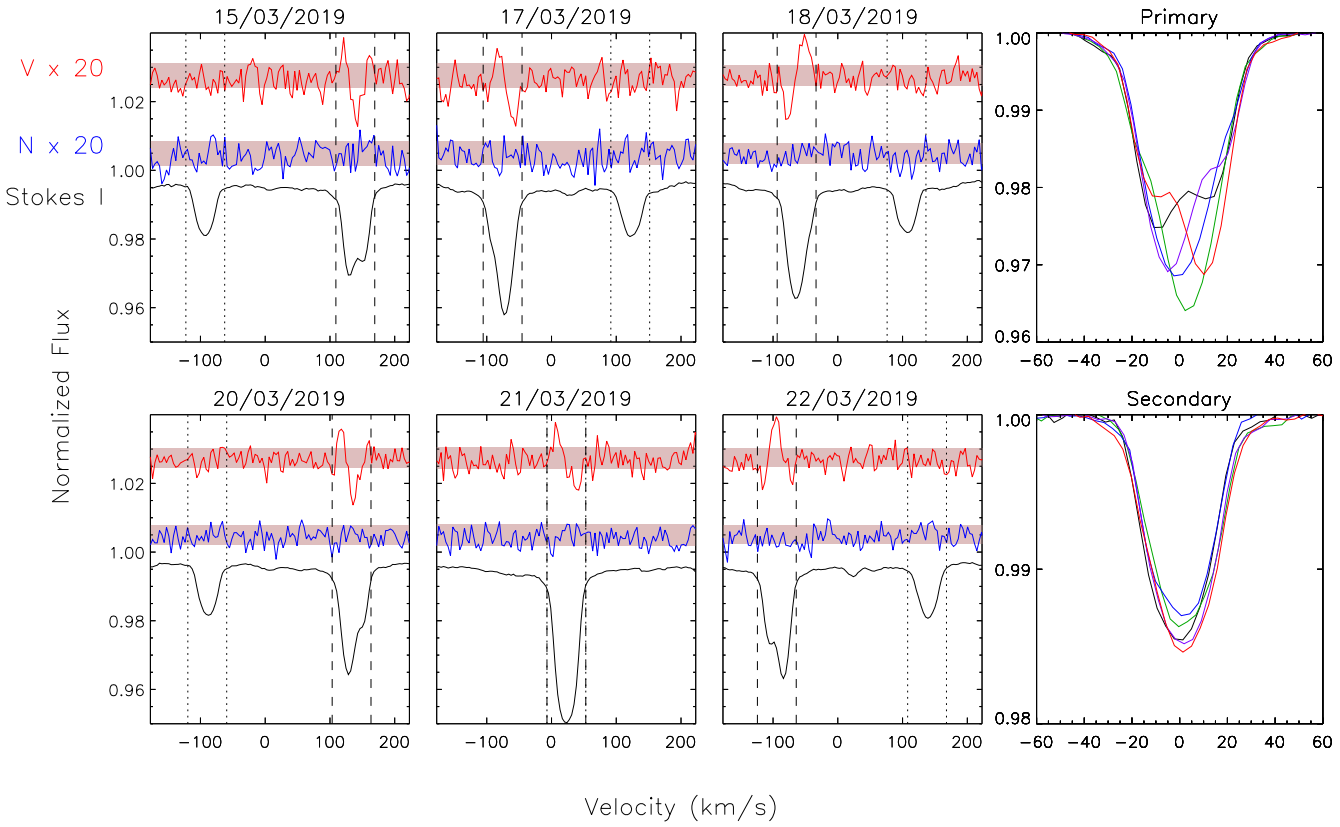

Figure 2. LSD profiles extracted from ESPaDOnS spectra. Grey shaded regions indicate ± the mean uncertainty. Vertical dashed lines indicate the integration limits of the primary's line profile, dotted lines show the same for the secondary. The two panels on the right show close-ups of the Stokes I LSD profiles of the two components at non-eclipsing phases, shifted to their respective rest frames.

Table 4. Table of RV and $\langle B_z \rangle$ measurements.'DF' is the detection flag (described in more detail in the text).

		Primary			Secondary		
HJD - 2458500	Date	RV (km s^{-1})	$\langle B_z \rangle$ (G)	DF	RV (km s^{-1})	$\langle B_z \rangle$ (G)	DF
57.74908	15/03/2019	139	37 ± 51	DD	-92	31 ± 83	ND
59.74646	17/03/2019	-73	121 ± 39	DD	121	73 ± 79	ND
60.74559	18/03/2019	-63	-258 ± 39	DD	106	165 ± 75	ND
62.74468	20/03/2019	133	102 ± 34	DD	-89	-135 ± 62	ND
63.72817	21/03/2019	22	96 ± 26	MD	22	–	–
64.81290	22/03/2019	-93	13 ± 34	DD	137	2 ± 58	ND

tator model parameters, we utilized the Hertzsprung-Russell Monte Carlo sampler described by Shultz et al. (submitted), adopting the radius from the orbital PHOEBE model, with the luminosity inferred from R_* and $T_{\rm eff}$, and $v \sin i$ as determined from the fits to the LSD Stokes I profiles. This yielded $i_{\rm rot} = 79^\circ \pm 6$, which is within 1σ of $i_{\rm orb}$, consistent with the spin and orbital axes being aligned. The obliquity angle of the magnetic from the rotational axis is $\beta = 86^{\circ\,+14}_{-22}$. The surface strength of the magnetic dipole is $B_{\rm d} = 880^{+780}_{-160}$ G, where we used the observational $\langle B_z \rangle_{\rm max} = -258 \pm 39$ G and the linear limb darkening coefficient $\epsilon = 0.47$ from the LTE tables calculated by Díaz-Cordovés et al. (1995).

To place upper limits on $B_{\rm d}$ for the non-magnetic star, we assumed that $i_{\rm rot}$ is within 10° of $i_{\rm orb}$, and adopted the same value of ϵ as for the magnetic star. This assumption is justified given that 1) $v \sin i$ is very similar between the two components, and 2) the value of $\omega_{\rm rot}/\omega_{\rm orb}$ inferred from PHOEBE modelling is very close to 1. $B_0 = 10 \pm 30$ G and $B_1 = 100 \pm 40G$ were taken respectively the weighted mean and weighted standard deviation of $\langle B_z \rangle$, with $\langle B_z \rangle_{\rm max}$ set to the same value as B_1. This yielded 1 and 3σ upper limits on $B_{\rm d}$ of 700 G and 1500 G, similar to the value inferred for the magnetic star. Therefore, on the basis of $\langle B_z \rangle$ alone

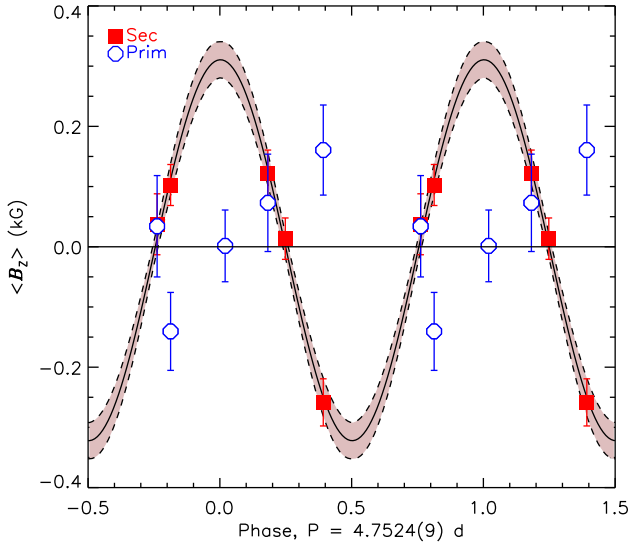

Figure 3. Out-of-eclipse $\langle B_z \rangle$ measurements for the two components, phased with the orbital period. The solid curve shows the best-fit sinusoid; the dashed curves show the 1σ uncertainties in the fit.

it cannot be ruled out that the non-magnetic star has a magnetic field approximately as strong as the magnetic star.

4.2 Bayesian analysis of line profiles

As a more precise means of constraining the surface magnetic fields of the two stars, we modelled their Stokes V profiles using RAVEN, the Bayesian inference method described by Petit & Wade (2012). We adopted the same $v \sin i$ values and limb darkening as determined above. The observation obtained on 21/03/2019 was excluded as the secondary was eclipsing the primary at this time.

For the secondary, this analysis finds 1, 2, and 3σ upper limits on B_d of 110 G, 340 G, and 1260 G. This star is thus almost certainly below the 300 G critical field limit identified by Aurière et al. (2007)'s survey of weak-field Ap/Bp stars (and verified by Sikora et al. 2019b's volume limited survey of Ap stars). As such, if the star has a magnetic field it is likely to be of the ultra-weak variety exhibited by Vega, Sirius, or Alhena (Petit et al. 2010, 2011; Blazère et al. 2016).

For the primary we initially performed a fit without constraints on P_rot or i_rot, obtaining maximum-likelihood values for i, β, and B_d of about 90°, 75°, and 500 G. The method therefore strongly prefers a large i_rot and β, with the former consistent with expected spin-orbit alignment.

In an effort to improve the constraints, we next utilized CROW, a modified version of RAVEN that includes rotational phase information. We also fixed $i_\mathrm{rot} = i_\mathrm{orb} = 84° \pm 1$. The resulting fit to Stokes V is shown in Fig. 4. This yielded $\beta = 94°$, with 1, 2, and 3σ uncertainties of 23°, 46°, and 60°. For B_d we obtained a maximum likelihood of 650 G, with upper uncertainties of 150 G, 400 G, and 1000 G, and lower uncertainties of 50 G, 100 G, and 150 G.

CROW obtains similar values of β and B_d to those inferred from modelling $\langle B_z \rangle$, with the two overlapping at the 1σ level. In contrast to the constraints from $\langle B_z \rangle$, direct

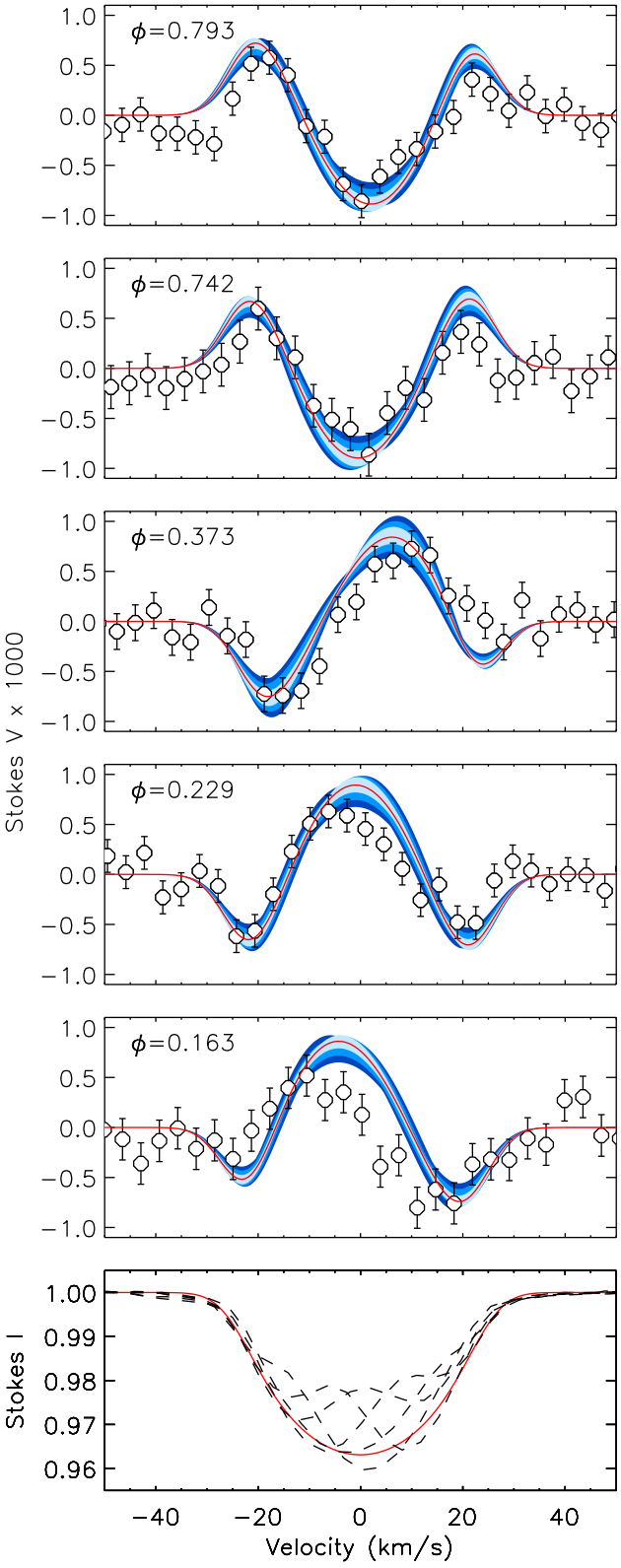

Figure 4. Fits to Stokes V from Bayesian modelling. Stokes I is shown in the bottom panel (observed - dashed black; synthetic, solid red). The top five panels show Stokes V, with the rotation phase ϕ indicated in the top left corner. Observed Stokes V is shown by open circles. The best-fit model is indicated by solid red lines; 1, 2, and 3σ uncertainties are indicated by light blue, blue, and dark blue shaded regions.

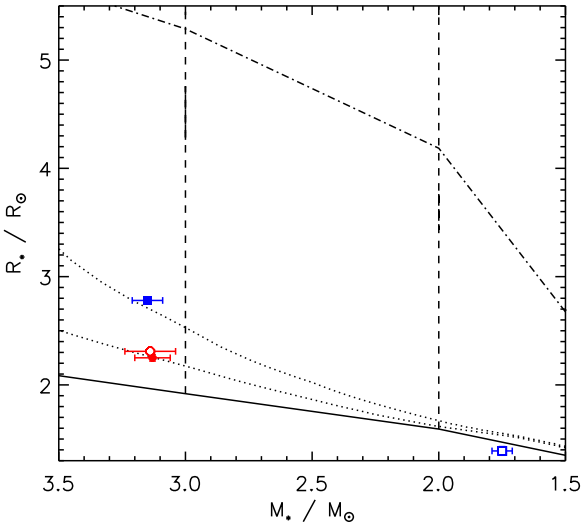

Figure 5. Mass-radius diagram. The ZAMS and TAMS are shown by solid and dot-dashed lines; rotating evolutionary models (Ekström et al. 2012) by dashed lines; $\log t = 8$ and 8.3 Myr isochrones by dotted lines. HD 62658 is indicated by red circles, HD 66051 by blue squares; magnetic and non-magnetic components by filled and open symbols.

modelling of Stokes V is able to demonstrate that the magnetic field of the non-magnetic star is much weaker than that of the magnetic star, with the difference significant at the 2σ level.

5 DISCUSSION

Fig. 5 compares the derived stellar parameters of HD 62658 and HD 66051 to evolutionary models (Ekström et al. 2012). The HD 62658 components have the same mass as the magnetic component of HD 66051, but are somewhat younger ($\log t = 8$ vs. 8.3 Myr). In contrast to HD 66051, which has a mass ratio of $M_2/M_1 = 0.55$, the components of HD 62658 are essentially identical in mass. Indeed, while there are several magnetic close binary systems with mass ratios much closer to 1 than that of HD 66051, e.g. HD 149277 (q=0.91; Shultz 2016; González et al. 2018) and ϵ Lupi (q=0.83; Pablo et al. 2019), the mass ratio of HD 62658 is the closest to unity of any other known magnetic hot binary.

In addition to having essentially identical masses, HD 62658's components are presumably coeval (e.g. White & Ghez 2001). Their rotational velocities are furthermore almost the same. They apparently differ only in that one of the stars has a fossil magnetic field, and the other does not. This remarkable object may have implications for our understanding of the formation of fossil magnetic fields, and the relation of the originating process to the overall rarity of magnetic stars in close binary systems. As noted in the introduction, hypotheses seeking to explain the rarity of such systems include:

(i) Magnetization of the protostellar cloud provides the seed for the fossil field, and also inhibits fragmentation of the cloud and therefore prevents the formation of binaries (Commerçon et al. 2011)

(ii) Fossil fields are left over from dynamos powered by stellar mergers (Schneider et al. 2016)

(iii) Tidal interactions in eccentric binaries lead to the rapid decay of fossil magnetic fields (Vidal et al. 2019)

The existence of some, rather than no, close binaries including at least one star with a fossil field suggests that i) is unlikely to be universally true. While ii) cannot be ruled out in all cases, it can probably be excluded in magnetic close binaries, since stellar mergers would be unlikely to leave behind a close binary of any sort, especially a circularized and tidally locked system, of which a handful are known (e.g. HD 66051, HD 156324 Kochukhov et al. 2018; Shultz et al. 2018a).

Since the mechanism suggested in scenario iii) requires variable tidal forces due to an eccentric orbit, it cannot be operating in this case. However, assuming that the system was not always circularized, it may have been operating in the past. The total unsigned magnetic flux is $\log \Phi = \log (B_{\rm d} R_*^2) = 3.6 \pm 0.1$ G $R_\odot^2$. This is at the lower limit of the range of magnetic fluxes reported by Sikora et al. (2019b) for their volume-limited sample of Ap/Bp stars, which extended up to the mass range occupied by HD 62658. Since (Sikora et al. 2019b) found no evidence for flux decay in this mass range, HD 62658's magnetic flux is not obviously anomalous for its age.

The previously listed hypotheses for the origin of fossil fields, and their rarity amongst binaries, can broadly be classified as environmental (i.e. relating to the magnetic flux within the molecular cloud from which the star formed), or evolutionary (i.e. relating to some circumstance of the star's evolution after formation). The existence of system with stars that are identical in their fundamental parameters, and which must have formed in the same place and at the same time, calls these scenarios into question.

At the other end of the main sequence there is a magnetic dichotomy somewhat similar to that of hot magnetic stars with and without fossil fields, namely the bimodal distribution of M-dwarf magnetic field strengths and geometries reported by Shulyak et al. (2017). Briefly, some of these stars possess strongly organized poloidal fields with surface strengths above the 4 kG saturation limit, while others have tangled topologies with surface strengths well below this limit. This bimodal distribution is thought to be a consequence of a theoretical dynamo bistability explored by Gastine et al. (2013), who found that the rotational-convective dynamos of these stars could stabilize into one or the other topology.

Dynamo bistability is further strengthened by Zeeman Doppler Imaging maps of the visual M-dwarf binary BL Cet and UV Cet presented by (Kochukhov & Lavail 2017). These stars are nearly identical in mass and rotation, yet one possesses a globally organized, axisymmetric poloidal field, while the other has a much weaker, non-axisymmetric, tangled field. Persistent differences in stellar activity indices suggest that these different magnetic field structures are not do to the stars having been observed at different points in their magnetic activity cycles (Audard et al. 2003). The BL Cet/UV Cet system is thus remarkably similar to the case of HD 62658.

While fully convective M-dwarves with rotational-convective dynamos, and B stars with radiative envelopes and fossil magnetic fields, are very different in a number of important ways, intermediate mass stars pass through a fully convective phase during their pre-main sequence (PMS) evolution. During this period an intermediate mass star is, from a magnetohydrodynamic perspective, somewhat similar to an M dwarf. It is therefore reasonable to expect that intermediate mass stars may exhibit a similar dynamo bistability on the PMS. This may provide a natural explanation for the magnetic desert amongst hot stars, with 10% possessing strong, globally organized dipoles, and the majority no fields at all, or ultra-weak fields such as those observed on Vega, Sirius, and Alhena (Lignières et al. 2009; Petit et al. 2011; Blazère et al. 2016).

In this scenario, the fossil magnetic fields of those stars which fail to organize into dipoles rapidly decay due to rotationally induced instabilities (e.g. Aurière et al. 2007; Braithwaite & Cantiello 2013). Such a bistability scenario would naturally account for the magnetic desert, and does not invoke environmental factors (e.g. the magnetic flux inherited from the protostellar cloud); importantly, environmental factors seem to be ruled out as a plausible hypothesis for fossil field origin by the HD 62658 system, since the stars are identical in age, must have formed very close together, and are within 0.3% of being the same in mass.

6 CONCLUSIONS

We report the discovery via KELT photometry of the second chemically peculiar magnetic eclipsing binary system, HD 62658. Modelling of radial velocities and the TESS light curve reveals that the system is nearly circularized, and that the two components have almost identical masses of about 3 $M_{\odot}$. The out-of-eclipse variability is consistent with rotational modulation of chemical spots, and the evidence suggests that the rotation of the chemically peculiar component is synchronized with the orbit.

High-resolution spectropolarimtery reveals the system to be an SB2, as expected. One of the components exhibits strong line profile variations consistent with the presence of chemical spots. The other component exhibits weaker variations, which may be consistent with gravity-mode pulsations detected in the light curve. A magnetic field with is detected in the chemically peculiar component; $\langle B_z \rangle$ phases coherently with the rotational period inferred from the light curve. Assuming a dipolar oblique rotator model, the magnetic component possesses a surface dipole strength of about 700 G. No magnetic field is detected in the other component, and direct modelling of its circular polarization profile indicates a surface dipole field below about 100 G.

The existence of two coeval stars with identical fundamental parameters, which formed in the same environment, and differ only in that one is magnetic, suggests that environmental or evolutionary scenarios for the origin of fossil fields and their rarity in binary systems may be mistaken, and that the explanation of these phenomena may instead by found in a pre-main sequence dynamo bistability similar to that identified in M-dwarfs. It is, however, essential that further observations of this system be obtained, in order to improve the constraints on the magnetic field of the secondary and definitively rule out the presence of a magnetic field on this star.

This system represents a unique opportunity to compare stellar structure models of stars with and without strong magnetic fields, and may be important for exploration of the consequences of fossil magnetism above and beyond the presence of chemical spots. Such investigations will require detailed knowledge of the magnetic star's surface magnetic field topology and chemical element distribution.

ACKNOWLEDGEMENTS

This work has made use of the VALD database, operated at Uppsala University, the Institute of Astronomy RAS in Moscow, and the University of Vienna. This work is based on observations obtained at the Canada-France-Hawaii Telescope (CFHT) which is operated by the National Research Council of Canada, the Institut National des Sciences de l'Univers of the Centre National de la Recherche Scientifique of France, and the University of Hawaii. This research has made use of the SIMBAD database, operated at CDS, Strasbourg, France. Some of the data presented in this paper were obtained from the Mikulski Archive for Space Telescopes (MAST). STScI is operated by the Association of Universities for Research in Astronomy, Inc., under NASA contract NAS5-2655. MES acknowledges support from the Annie Jump Cannon Fellowship, supported by the University of Delaware and endowed by the Mount Cuba Astronomical Observatory. ADU acknowledges support from the National Science and Engineering Research Council of Canada (NSERC). GAW acknowledges support from a Discovery Grant from NSERC. CJ acknowledges funding from the European Research Council (ERC) under the European Union's Horizon 2020 research and innovation programme (grant agreement N°670519: MAMSIE), as well as from the Research Foundation Flanders (FWO) under grant agreement G0A2917N (BlackGEM). CJ acknowledges the use of computational resources and services provided by the VSC (Flemish Supercomputer Center), funded by the Research Foundation - Flanders (FWO) and the Flemish Government department EWI. OK acknowledges support by the Knut and Alice Wallenberg Foundation (project grant "The New Milky Way"), the Swedish Research Council (project 621-2014-5720), and the Swedish National Space Board (projects 185/14, 137/17).

REFERENCES

Alecian E., et al., 2015, in New Windows on Massive Stars. pp 330–335 (arXiv:1409.1094), doi:10.1017/S1743921314007030
Astropy Collaboration et al., 2013, A&A, 558, A33
Audard M., Güdel M., Skinner S. L., 2003, *ApJ*, 589, 983
Aurière M., et al., 2007, A&A, 475, 1053
Blazère A., Neiner C., Petit P., 2016, *MNRAS*, 459, L81
Braithwaite J., Cantiello M., 2013, *MNRAS*, 428, 2789
Collins K. A., et al., 2018, *AJ*, 156, 234
Commerçon B., Hennebelle P., Henning T., 2011, *ApJL*, 742, L9
David-Uraz A., et al., 2019, *MNRAS*, 487, 304

Degroote P., et al., 2009, A&A, 506, 111
Díaz-Cordovés J., Claret A., Giménez A., 1995, A&AS, 110, 329
Donati J.-F., Semel M., Rees D. E., 1992, A&A, 265, 669
Donati J.-F., Semel M., Carter B. D., Rees D. E., Collier Cameron A., 1997, MNRAS, 291, 658
Ekström S., et al., 2012, A&A, 537, A146
Foreman-Mackey D., Hogg D. W., Lang D., Goodman J., 2013, PASP, 125, 306
Gastine T., Morin J., Duarte L., Reiners A., Christensen U. R., Wicht J., 2013, A&A, 549, L5
Glagolevskij Y. V., 1994, Bulletin of the Special Astrophysics Observatory, 38, 152
González J. F., Hubrig S., Järvinen S. P., Schöller M., 2018, *MNRAS*, 481, L30
Grunhut J. H., et al., 2017, *MNRAS*, 465, 2432
Jenkins J. M., et al., 2016, in Software and Cyberinfrastructure for Astronomy IV. p. 99133E, doi:10.1117/12.2233418
Kochukhov O., Lavail A., 2017, *ApJL*, 835, L4
Kochukhov O., Makaganiuk V., Piskunov N., 2010, A&A, 524, A5
Kochukhov O., Johnston C., Alecian E., Wade G. A., 2018, *MNRAS*, 478, 1749
Kochukhov O., Shultz M., Neiner C., 2019, A&A, 621, A47
Kupka F. G., Piskunov N., Ryabchikova T. A., Stempels H. C., Weiss W. W., 1999, A&AS, 138, 119
Kupka F. G., Ryabchikova T. A., Piskunov N. E., Stempels H. C., Weiss W. W., 2000, Balt. Astron., 9, 590
Landstreet J. D., Kochukhov O., Alecian E., Bailey J. D., Mathis S., Neiner C., Wade G. A., BINaMIcS Collaboration 2017, A&A, 601, A129
Lignières F., Petit P., Böhm T., Aurière M., 2009, A&A, 500, L41
Lomb N. R., 1976, ApSS, 39, 447
Mathys G., 1989, FCPh, 13, 143
Neiner C., Mathis S., Alecian E., Emeriau C., Grunhut J., BinaMIcS MiMeS Collaborations 2015, in Nagendra K. N., Bagnulo S., Centeno R., Jesús Martínez González M., eds, IAU Symposium Vol. 305, Polarimetry. pp 61–66 (arXiv:1502.00226), doi:10.1017/S1743921315004524
Pablo H., et al., 2019, *MNRAS*, 488, 64
Pepper J., et al., 2007, PASP, 119, 923
Pepper J., Kuhn R. B., Siverd R., James D., Stassun K., 2012, PASP, 124, 230
Petit V., Wade G. A., 2012, MNRAS, 420, 773
Petit P., et al., 2010, A&A, 523, A41
Petit P., et al., 2011, A&A, 532, L13
Piskunov N. E., Kupka F., Ryabchikova T. A., Weiss W. W., Jeffery C. S., 1995, A&AS, 112, 525
Preston G. W., 1967, *ApJ*, 150, 547
Price-Whelan A. M., et al., 2018, *AJ*, 156, 123
Prsa A., Matijevic G., Latkovic O., Vilardell F., Wils P., 2011, PHOEBE: PHysics Of Eclipsing BinariEs (ascl:1106.002)
Prša A., Zwitter T., 2005, *ApJ*, 628, 426
Renson P., Manfroid J., 2009, A&A, 498, 961
Ricker G. R., et al., 2015, Journal of Astronomical Telescopes, Instruments, and Systems, 1, 014003
Ryabchikova T. A., Piskunov N. E., Kupka F., Weiss W. W., 1997, Balt. Astron., 6, 244
Ryabchikova T., Piskunov N., Kurucz R. L., Stempels H. C., Heiter U., Pakhomov Y., Barklem P. S., 2015, Phys. Scr., 90, 054005
Sana H., et al., 2012, Science, 337, 444
Schneider F. R. N., Podsiadlowski P., Langer N., Castro N., Fossati L., 2016, *MNRAS*, 457, 2355
Shultz M., 2016, PhD thesis, Queen's University (Canada
Shultz M., Rivinius T., Wade G. A., Alecian E., Petit V., 2018a, *MNRAS*, 475, 839
Shultz M. E., et al., 2018b, *MNRAS*, 475, 5144
Shulyak D., Reiners A., Engeln A., Malo L., Yadav R., Morin J., Kochukhov O., 2017, Nature Astronomy, 1, 0184
Sikora J., Wade G. A., Power J., Neiner C., 2019a, *MNRAS*, 483, 2300
Sikora J., Wade G. A., Power J., Neiner C., 2019b, *MNRAS*, 483, 3127
Stassun K. G., et al., 2018, *AJ*, 156, 102
Vidal J., Cébron D., Ud-Doula A., Alecian E., 2019, arXiv e-prints,
Wade G. A., et al., 2016, *MNRAS*, 456, 2
White R. J., Ghez A. M., 2001, *ApJ*, 556, 265
Zahn J. P., 1975, A&A, 41, 329
Zahn J. P., 1977, Penetrative convection in stars. pp 225–234, doi:10.1007/3-540-08532-7˙45
Zechmeister M., Kürster M., 2009, A&A, 496, 577
de Mink S. E., Langer N., Izzard R. G., Sana H., de Koter A., 2013, *ApJ*, 764, 166
de Mink S. E., Sana H., Langer N., Izzard R. G., Schneider F. R. N., 2014, *ApJ*, 782, 7

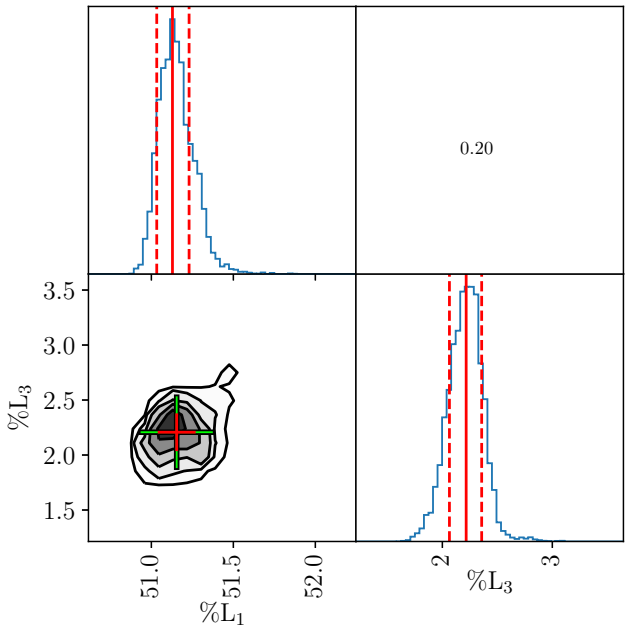

Figure A1. Marginalised posterior distributions for the light parameters from MCMC modelling.

APPENDIX A: POSTERIOR DISTRIBUTIONS

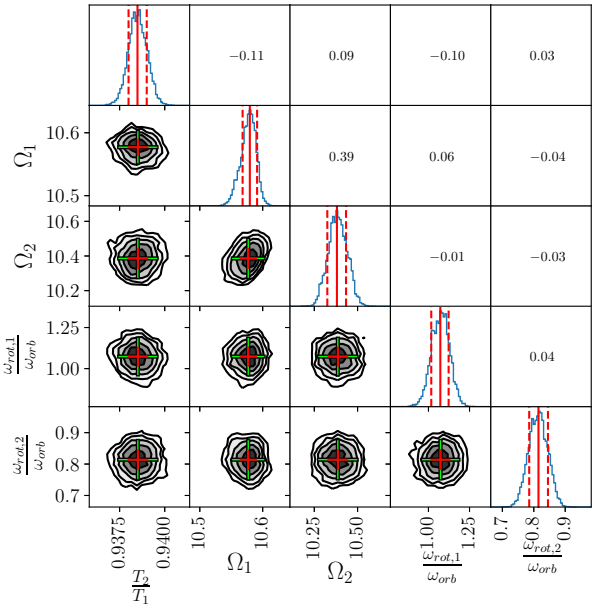

Figure A2. Marginalised posterior distributions for the stellar parameters from MCMC modelling.

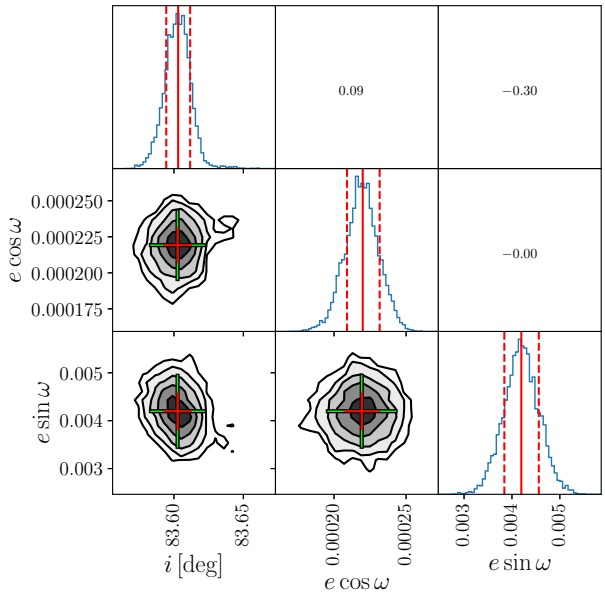

Figure A4. Marginalised posterior distributions for more orbital parameters from MCMC modelling.

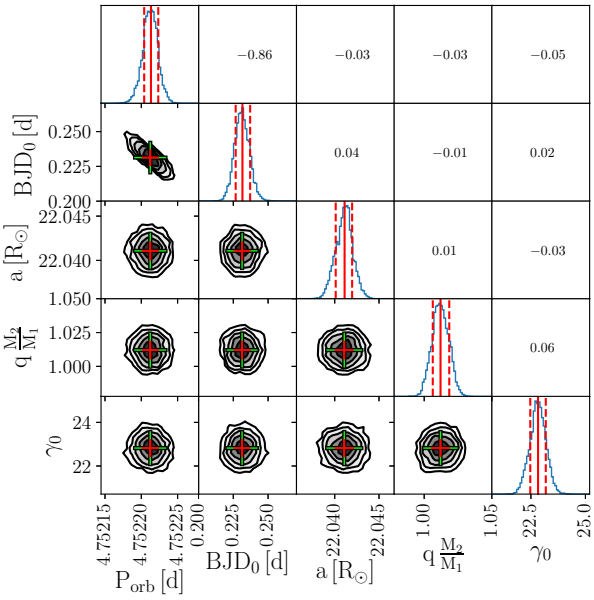

Figure A3. Marginalised posterior distributions for the orbital parameters from MCMC modelling.